



Highly efficient electrosynthesis of hydrogen peroxide through the combination of side aeration and vacuum filtration modified graphite felt

Mingran Li^a, Huachun Lan^b, Xiaoqiang An^b, Xia Qin^{a,*}, Zilong Zhang^a, Tinghui Li^a

^a Faculty of Environment and Life, Beijing University of Technology, No.100 Pingleyuan, Chaoyang District, Beijing 100124, China

^b Center for Water and Ecology, State Key Joint Laboratory of Environment Simulation and Pollution Control, School of Environment, Tsinghua University, Beijing 100084, China

ARTICLE INFO

Keywords:

Hydrogen peroxide
Two electron oxygen reduction reaction
Oxygen mass transfer, alkaline preference
Graphite felt

ABSTRACT

The electrocatalytic activity towards two electron oxygen reduction reaction of graphite felt was advanced by incorporating carbon nitride, carbon nanotubes and polytetrafluoroethylene through vacuum filtration, which prevented the cleavage of O-O bond, facilitated the charge transfer, and established more three-phase active sites. To ameliorate the oxygen transfer process, the configuration of side-aeration was proposed, providing forced convection to reduce the thickness of diffusion layer, and increasing the dissolved oxygen. By simplified combination of refining the orientation of gas flow and modified graphite felt, the dual-chamber configuration rendered a qualitative leap in H₂O₂ generation capacity to 4.44–6.89 mg h⁻¹ cm⁻². The alkaline affinity of developed system was discussed in terms of a beneficial outer-sphere electron transfer pathway, the variation on adsorption strength of oxygenated species and working electrode potential range. Finally, Long-term operation stability and successful application in Electro-Fenton indicated great potential of developed system for H₂O₂ synthesis and environmental remediation.

1. Introduction

Hydrogen peroxide (H₂O₂) is a green oxidant and energy carrier applied in the fields of pulp bleaching, disinfection, chemical synthesis, and environmental remediation. Specifically, H₂O₂ could effectively degrade organic pollutants through hydroxyl radical-involved Fenton reaction, in which the oxidation product of H₂O₂ is water in accordance with the stringent requirement of green and sustainable development [1]. To date, 90 % industrial-scale production of H₂O₂ is achieved via multistep processes of consecutive anthraquinone hydrogenation and oxidation [2]. However, this process faces the issues of energy-consuming, huge infrastructure, considerable waste, unsafety in the transportation and storage of H₂O₂, which stimulates the requirement of on-site production and utilization of H₂O₂. In this context, there has been mounting interests to investigate electrochemical two-electron oxygen reduction reaction (2e⁻ ORR) as an effective route to achieve decentralized production of H₂O₂.

ORR occurring at the cathode is acknowledged to proceed via “parallel” routes with the 4e⁻ pathway and 2e⁻ pathway with H₂O (OH⁻) (Eqs. 1 and 3) or H₂O₂ (HO₂⁻) (Eqs. 2 and 4) as the final product, respectively [3]. Therefore, the development of electrocatalysts and cathode

materials with a high activity and selectivity towards the 2e⁻ ORR has become a paramount issue. Thus far, extensive electrocatalysts have been devised to facilitate the production of H₂O₂, encompassing noble metals, single-atom catalysts, conducting polymers, organic coordination compounds, metal compounds, and carbon-based materials [4–7]. Among these electrocatalysts, carbonaceous materials stand out as the prevailing choice in electrochemical processes employed for water treatment due to high abundance, low cost, acceptable stability, and environmental compatibility; examples include hierarchically porous carbon, carbon nanotubes and graphitized carbon nanohorns. Apart from nanostructured catalysts, commercially available materials, such as active carbon fiber (ACF), reticulated vitreous carbon, graphite plate and graphite felt (GF) is extensively explored for pilot scale applications [8–14]. Compared with ACF that we investigated before, GF offers better conductivity, higher hydrophobicity and hardness to ensure the robust stability, which renders it a more suitable candidate as a carbonaceous substrate. Nevertheless, the primary hindrance impeding the practical environmental implementation of on-site oxygen reduction reaction (ORR) is its inadequate production capacity of H₂O₂, which fails to meet the demands of actual environmental treatment technologies, particularly in the case of Fenton technology (Table S1). Hence, improving the

* Corresponding author.

E-mail address: qinxia@bjut.edu.cn (X. Qin).

<https://doi.org/10.1016/j.apcatb.2023.123125>

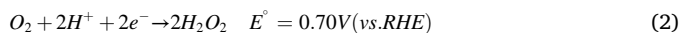
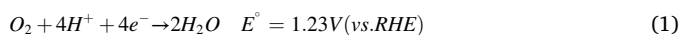
Received 18 April 2023; Received in revised form 25 June 2023; Accepted 20 July 2023

Available online 22 July 2023

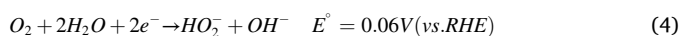
0926-3373/© 2023 Elsevier B.V. All rights reserved.

electrochemical activity of cathode materials towards $2e^-$ ORR becomes a prerequisite for actual environmental applications.

In acidic medium,



In alkaline medium,



In this work, a multitude of N-functional sites brought by graphitic carbon nitride (g-C₃N₄) advances the “end-on” adsorption of oxygen and modulates the binding capability of *OOH, curbing the cleavage of O-O bond during the ORR. Maintaining O-O bond in O₂ or *OOH effectively steers the ORR selectivity towards $2e^-$ pathway [12]. Considering the confined electron transfer ability of g-C₃N₄, the introduction of carbon nanotubes (CNTs) as three dimensional conductive support in catalytic layer facilitates the charge transfer, which enables the sufficient utilization of active sites [15]. The exposed edge plane defects and oxygen-containing functional groups on the oxidized multi-walled CNTs further enhances the adsorption of reactive intermediates in $2e^-$ ORR [13]. Introducing appropriate amount of polytetrafluoroethylene (PTFE) contributes to the establishment of gas-liquid-solid three-phase interfaces (TPIs) equilibrium, which facilitates the electrode to direct utilize the oxygen from the gas film adhered on its surface [16]. A synthesis strategy of vacuum filtration-calcination for modifying GF is proposed to overcome the defects in impregnation method. The powerful pumping force provided by vacuum filtration promotes insoluble g-C₃N₄ and CNTs more uniformly and firmly fasten on the top surface of graphite felt and develops a deeper catalytic layer with a certain gradient.

In the face of the challenges posed by the treatment of wastewater with high inflow rates or the addition of substantial amounts of H₂O₂ in practical applications for electrochemical synthesis of H₂O₂, it becomes imperative to consider the relationship between applied current density and the electrode area, as described by Eq. 5. The majority of current densities investigated in submerged and aerated electrode (SAE) studies at the laboratory scale (approximately 0.4–1.5 mA cm⁻²) prove inadequate for such actual applications due to the prohibitive difficulties associated with constructing and operating reactors brought by corresponding extremely large electrode area [17]. Consequently, the enhancement of current density is crucial for scaling up and practical application for electrosynthesis of H₂O₂. Nonetheless, when the current density reaches a certain threshold (typically exceeding 10 mA cm⁻²), the gas film disappears, resulting in oxygen diffusion occurring solely through dissolved oxygen (DO). ORR of the SAE is prone to mass transfer controlled regime due to the limited solubility (8.1–8.5 mg/L) and diffusivity ($1.96\text{--}2.56 \times 10^{-9} \text{ m}^2 \text{ s}^{-1}$) of DO with a poor oxygen utilization efficiency (OUE, usually <1 %), leading to an escalation in undesired hydrogen evolution side-reactions and subsequent reduction of H₂O₂ [18–20]. Consequently, the generation rate of H₂O₂ experiences a decline, and in some cases, the deactivation of electrodes may occur. To ameliorate the O₂ mass transfer, multiple strategies have been attempted, including a jet reactor inspired by venturi effect [21], a novel floating cathode utilizing additional oxygen in air [22], a simple method just conducted in higher pressure [18], a micro-bubble assisted rotary cylinder electrode [23], filter-press flow cell [24] and extensively discussed gas diffusion [25] electrodes (GDE) [1,20,26]. However, these attempts for H₂O₂ production are constrained by the energy loss incurred from pressurization, intricacy of the reactor and high-priced electrode preparation, as well as inferior stability. To strike a balance from these issues, a simplified combination of SAE and side aeration is proposed, which provides a qualitative leap in the electro-generation of

H₂O₂ through reducing the thickness of diffusion layer and increasing the DO concentration.

$$1577QC = j\eta S \quad (5)$$

Where Q is flow rate of wastewater (m³/h), C is amount of H₂O₂ (mg/L), j is current density (mA/cm²), η is the current efficiency of electrode, S is electrode area (cm²).

In this study, we proposed a synthesis strategy of vacuum filtration-calcination to modify GF with g-C₃N₄, CNTs and PTFE. The correlation of electrocatalysts, vacuum filtration-calcination times, doping amount of PTFE with electrocatalytic performance towards $2e^-$ ORR is achieved through a series of physicochemical and electrochemical measurements. To address the confined oxygen mass-transfer efficiency in ORR, a side-aeration configuration was established. The influential factors in electrocatalytic $2e^-$ ORR were profoundly discussed from the perspective of thermodynamics and electrochemical interface, particularly emphasizing on alkaline affinity of developed electrocatalytic system, which was extrapolated to a beneficial outer-sphere electron transfer pathway, the variation on adsorption strength of oxygenated species and working electrode potential range. Finally, long-term operation stability and successful application in the Electro-Fenton process indicated great potential of side-aeration configuration coupled with modified GF for H₂O₂ synthesis and environmental remediation.

2. Experimental section

2.1. Materials preparation

Commercially available graphite felts (Shanghai Qijie Carbon Material Co., Ltd) with the thickness of 2 mm were employed for structure modulation. Multi-walled carbon nanotubes (MWCNTs) were provided by Chengdu Institute of Organic Chemistry, Chinese Academy of Sciences. The acid-assisted chemical oxidation of MWCNTs and fabrication of g-C₃N₄ were depicted in Text S1. All other chemicals used were of analytical grade, unless otherwise specified, and acquired from commercial suppliers.

2.2. Synthesis of gc-GF electrode

A two-step procedure of vacuum filtration-calcination was employed for the fabrication of a multilayer g-C₃N₄ and CNTs modified electrode, the schematic representation of which is depicted in Fig.S1. Specifically, 90 mg of CNTs, 30 mg of g-C₃N₄ and 0.5 ml of 60 wt% PTFE dispersion were blended in 30 ml of deionized water for 5 min within a sonification equipment (Biosafe). The GF ultrasonically degreased by acetone for 2 h was cut into a circular shape with a diameter of 5 cm, which was tightly and flatly affixed at the bottom of filter cup with a 0.45 μm membrane positioned in the middle of GF and sand filtration layer. The well-mixed dispersion was poured into filter cup, following by vacuum filtration at the pressure of 0.08 MPa. After removed moisture at oven, the GF was transferred to the muffle furnace and calcined at 350 °C for 60 min with a heating rate of 5 °C/min. Upon cooling to room temperature, the obtained electrode was marked as gc-GF_{1 time}. The gc-GF_{2 times} and gc-GF_{3 times} were prepared by repetition of vacuum filtration-calcination 2 or 3 times. To discuss the effect of PTFE doping amount, the same procedure (vacuum filtration-calcination 2 times) was applied to gc-GF_{0 PTFE}, gc-GF_{0.1 PTFE}, gc-GF_{0.3 PTFE} and gc-GF_{0.7 PTFE} with a difference of 0, 0.1, 0.3, 0.7 ml 60 wt% PTFE dispersion added. For the sake of convenience, gc-GF_{2 times} or gc-GF_{0.5 PTFE} was substituted by gc-GF in the following text. The impregnation-calcination modified GF (gc-GF_{impregnation}) was followed the method described in the previous article and doping content of catalysts was the same with gc-GF_{1 time} [12]. Finally, the as-prepared electrode was cut into a dimension of 3 × 4 cm for subsequent utilization.

2.3. Materials characterization

Scanning electron microscopy (SEM) images were obtained on a Hitachi SU8020 microscope. SEM mapping images were obtained by combining with energy-dispersive X-ray spectroscopy system. The phase structure of electrode surface was studied using a Bruker D8 Advance X-ray diffractometer (XRD) with Cu K α as X-ray source ($\lambda = 1.5406 \text{ \AA}$, $2\theta = 2^\circ - 90^\circ$). The X-ray photoelectron spectroscopy (XPS) was carried out on an ESCALAB 250Xi spectrometer through Al K α radiation. Fourier-transformed infrared (FT-IR) spectroscopy was conducted on Bruker EQUINOX 55 spectrograph. N $_2$ adsorption-desorption isotherms were measured at 77 K with NOVA 3200e spectrometer. The surface areas were calculated with Brunauer-Emmett-Teller (BET) method and the pore distribution were analyzed based on Barrett-Joyner-Halenda (BJH) method. Raman spectra of prepared GF were collected on a confocal microscopic Raman spectrometer (Reinshaw inVia-Reflex, UK)

with 40 mW 532 nm laser light irradiation. The contact angle of water on the surface of electrode was measured by a drop shape analysis system (DSA100 KRÜSS). Zeta potential was determined by Zetasizer Nano instrument (Malvern, Nano Z). The solutions for zeta potential measurement were prepared by dissolving catalysts into ethanol. The conductivity of electrode was measured by the method of Four-Point probe (AT510). The details of electrochemical measurements were shown in Text S2.

2.4. Configuration of side-aeration reactor and electrochemical experiments

The schematic diagram of novel side-aeration reactor with dual chamber was illustrated in Fig. 1a), which was composed of two stackable modular units. The proton exchange membrane (Nafion®117) was utilized to separate anodic and cathodic chamber, in which IrO $_2$ /RuO $_2$ /

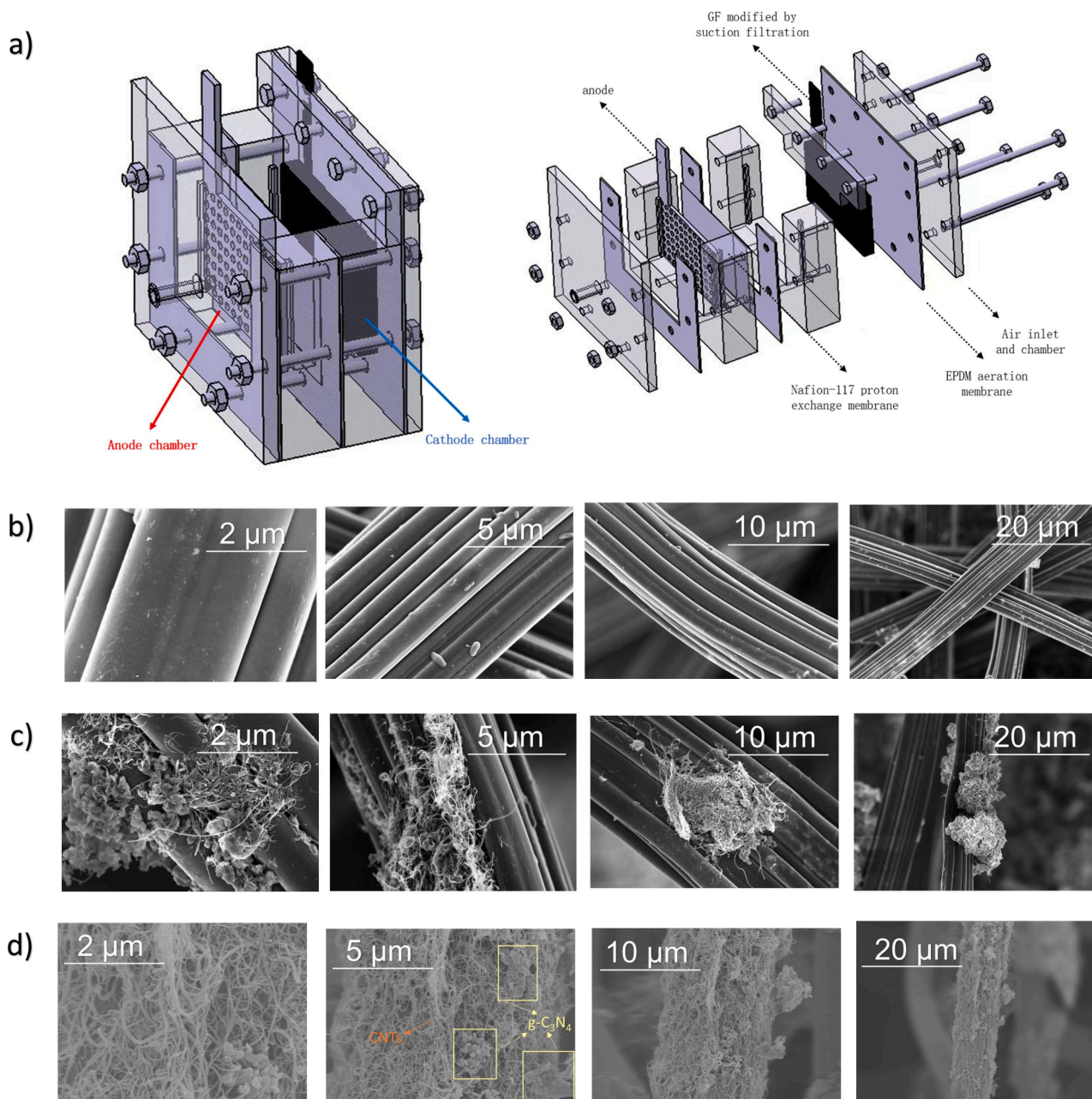


Fig. 1. a) The schematic diagram of side-aeration reactor; SEM images of b) pristine GF, c) GF modified by impregnation and d) GF modified by vacuum filtration-calcination.

Ti mesh acted as anode and gc-GF served as cathode. A parallel arrangement is implemented, whereby an ethylene propylene diene monomer (EPDM) membrane, serving as the oxygen supplier, is positioned alongside the inner wall of the cathodic chamber. Simultaneously, the catalytic layer of gc-GF is deliberately oriented towards the aeration membrane. The electrochemical process was carried out by charging with constant current. Initial pH was adjusted with H_2SO_4 and NaOH. Both compartments were filled with 50 ml 0.05 M Na_2SO_4 as electrolyte. Electro-Fenton (EF) experiments were conducted with a 100 mg/L concentration of different organic contaminants, including 2,4-dichlorophenoxyacetic acid (2,4-D), tetracycline (TC), phenol and bisphenol A (BPA), at constant current of 0.4 A, initial pH of 5, and 4 g/L of heterogeneous Fenton catalysts prepared by the reported methods [27]. All EF experiments were conducted in the same experimental setup for the electro-synthesis of H_2O_2 .

2.5. Analytical method

The sample of solution was taken from cathodic chamber at certain intervals. Produced H_2O_2 (HO_2) was quantified by potassium titanium (IV) oxalate method [12]. All the analyses were conducted in duplicate, and the average value was reported. The concentration of 2,4-D, TC, phenol, and BPA was analyzed by high-performance liquid chromatography (U3000, ThermoFisher) with a DAD detector (details in Text S3). Total organic carbon (TOC) was obtained by TOC-L (Shimadzu). Instantaneous production of $\cdot\text{OH}$ were detected by (Electron Spin Resonance) ESR spectra (Bruker A200 S-9.5/12 spectrometer) with DMPO as the target as the trapping agent and accumulated $\cdot\text{OH}$ was certified by photoluminescence method with coumarin as prob. The intensity of $\cdot\text{OH}$ was scanned at excitation wavelength of 332 nm [28]. The relative calculations were shown in Text S4.

3. Results and discussion

3.1. Characterization of GF modified by vacuum filtration

The morphologies of raw GF, gc-GF_{impregnation} and gc-GF were investigated by SEM. As shown in Fig. 1b) at different magnifications, the pristine GF displayed a smooth surface with almost no defects and formed interconnected network structure. The modification by impregnation encountered inferior load performance, which doping compounds aggregately adhered on the partial of GF (Fig. 1c)). Differ from gc-GF_{impregnation}, vacuum filtration ensured that the whole graphite felt was enclosed with doping catalysts (Fig. 1d) and Fig.S3). A multitude of tubular materials circumscribing GF surface elucidated the presence of CNTs in catalytic layer. Both bulk and 2D parallel morphologies of g- C_3N_4 were significantly observed on the GF (Fig. S4). As analyzed by the results of EDS (Fig.S5 and Table S2), the homogeneously distributed nitrogen element (13.82 wt%) and fluorine element (1.30 wt %) on the graphite felt estimated the successful load of g- C_3N_4 and PTFE.

The pore property of GF was characterized by N_2 adsorption-desorption experiment. It should be noted that nitrogen adsorption-desorption isotherm data of raw GF was missed due to the smooth surface of GF, which was lower than the detection limit of adsorbed N_2 quantity. All of modified GF had similar nitrogen adsorption-desorption isotherms which corresponded to the non-typical type IV curve with a

clear hysteresis loop and a capillarity condensation step at relatively high P/P_0 range from 0.65 to 1.0 (Fig.S5). According to the IUPAC, hysteresis loops of modified GF were affiliated with H_3 genre, which signified the predominant shape of multi-hierarchical parallel plate slit pore and the characteristic of mesopores and macropores. The introduction of 3D tubular CNTs, bulk and 2D parallel-plate g- C_3N_4 and phase transformation of PTFE during the calcination process established the porosity structure among the interconnected network, thus the surface area of all modified GF appeared considerable enlargement compared with sleekly raw GF ($3.24 \text{ m}^2 \text{ g}^{-1}$). As shown in inset of Fig. S5 and Table 1, gc-GF_{2 times} ($36.15 \text{ m}^2 \text{ g}^{-1}$, $0.11 \text{ cm}^3 \text{ g}^{-1}$) achieved more remarkable surface area and pore volume than those of gc-GF_{1 time} ($13.75 \text{ m}^2 \text{ g}^{-1}$, $0.077 \text{ cm}^3 \text{ g}^{-1}$) and gc-GF_{3 times} ($25.68 \text{ m}^2 \text{ g}^{-1}$, $0.041 \text{ cm}^3 \text{ g}^{-1}$). There was an evident diminishment in both surface area and pore volume of gc-GF_{3 times}, likely due to the filling of generated porosity with substantial catalysts during the third vacuum filtration process. Interestingly, the originally smooth GF after introducing catalysts exhibited a wider pore size distribution in the range from 1 to 55 nm. The average pore size of gc-GF_{2 times} centered around the diameter of 22.88 nm. Sufficient existence of mesopores and macropores ($V_{\text{meso+macro}} = 0.1008 \text{ cm}^3 \text{ g}^{-1}$) on the gc-GF played a paramount role in 2e^- ORR, which lowered the oxygen mass transfer hinderance [29].

To obtain more information about microstructure transformation, Raman spectra were collected and deconvoluted by mixed Lorentzian-Gaussian function. Two remarkable bands around 1345 (D peak) and 1570 (G peak) cm^{-1} referring to the characteristic graphene domain were observed. The ratio between the integral area of D and G band (I_D/I_G) was a semiquantitative parameter for assessing the number of defects related to the partial disruption of π -extended framework [9]. As shown in Fig. 2a), the value of I_D/I_G enlarged from 1.13 to 1.25 with the increase of vacuum filtration-calcination times, suggesting the growing of defect domain on the surface of electrode. Specifically, the defects sites were capable of attenuating the adsorption energy of active intermediates for 2e^- ORR [30]. The growth of defects could be extrapolated from two aspects: more defective sites brought by the intrinsic structure disorder in carbon lattice of growing CNTs and g- C_3N_4 and self-generation during repetitious calcination proceeding. Amorphous carbon regions of GF were more easily oxidized during annealing process and produced carbon dioxide exerted force against van der Waals bonding between internal structure of amorphous carbon, bringing about stripping partial area to create more exposure sites [31]. Negligible alterations of Raman spectra and obvious diffraction peaks of the (002) plane and (110) plane from XRD spectra (Fig.S6) served as evidences for the preservation of intact crystalline structure and conductivity of GF. Three peaks, attributed to PTFE, were visible after modification (at 18.2° , 18.7° and 22.6° , respectively). Moreover, the XRD patterns displayed identical diffractions of urea-derived carbon nitride centered at $2\theta = 16.5^\circ$, 27.9° , 32.2° and 37.2° .

The XPS spectra of raw GF and gc-GF was conducted to determine the elemental composition and functional groups of electrode surface (Fig. S7). The high resolution of N 1s spectrum was shown in Fig. 2b). For raw GF, the spectrum had two peaks at 358.58 eV and 401.08 eV, corresponded to pyridinic N and amine. The binding bonds of gc-GF could be assigned to pyridinic N (398.58 eV) and quaternary N (400.43 eV). The proportion of pyridinic N increased from 18 % to 50 % after modification. Pyridinic N was often postulated as the key feature for high ORR

Table 1

BET surface area, pore volume and average pore size for different modified GF.

	raw GF	gc-GF _{1 time}	gc-GF _{2 times} /gc-GF _{0.5 PTFE}	gc-GF _{3 times}	gc-GF _{0.1 PTFE}	gc-GF _{0.3 PTFE}	gc-GF _{0.7 PTFE}
$S_{\text{BET}} (\text{m}^2 \text{ g}^{-1})$	3.24	13.75	36.15	25.68	48.32	42.13	10.12
$V_{\text{tot}} (\text{cm}^3 \text{ g}^{-1})$	-	0.07732	0.11052	0.04129	0.11853	0.11264	0.10505
$V_{\text{meso+macro}} (\text{cm}^3 \text{ g}^{-1})$	-	0.05535	0.10077	0.03698	0.10021	0.10067	0.10084
$V_{\text{micro}} (\text{cm}^3 \text{ g}^{-1})$	-	0.00648	0.00866	0.00191	0.01833	0.01198	0.00421
Pore size (nm)	-	16.64	22.88	23.65	23.41	23.12	22.69

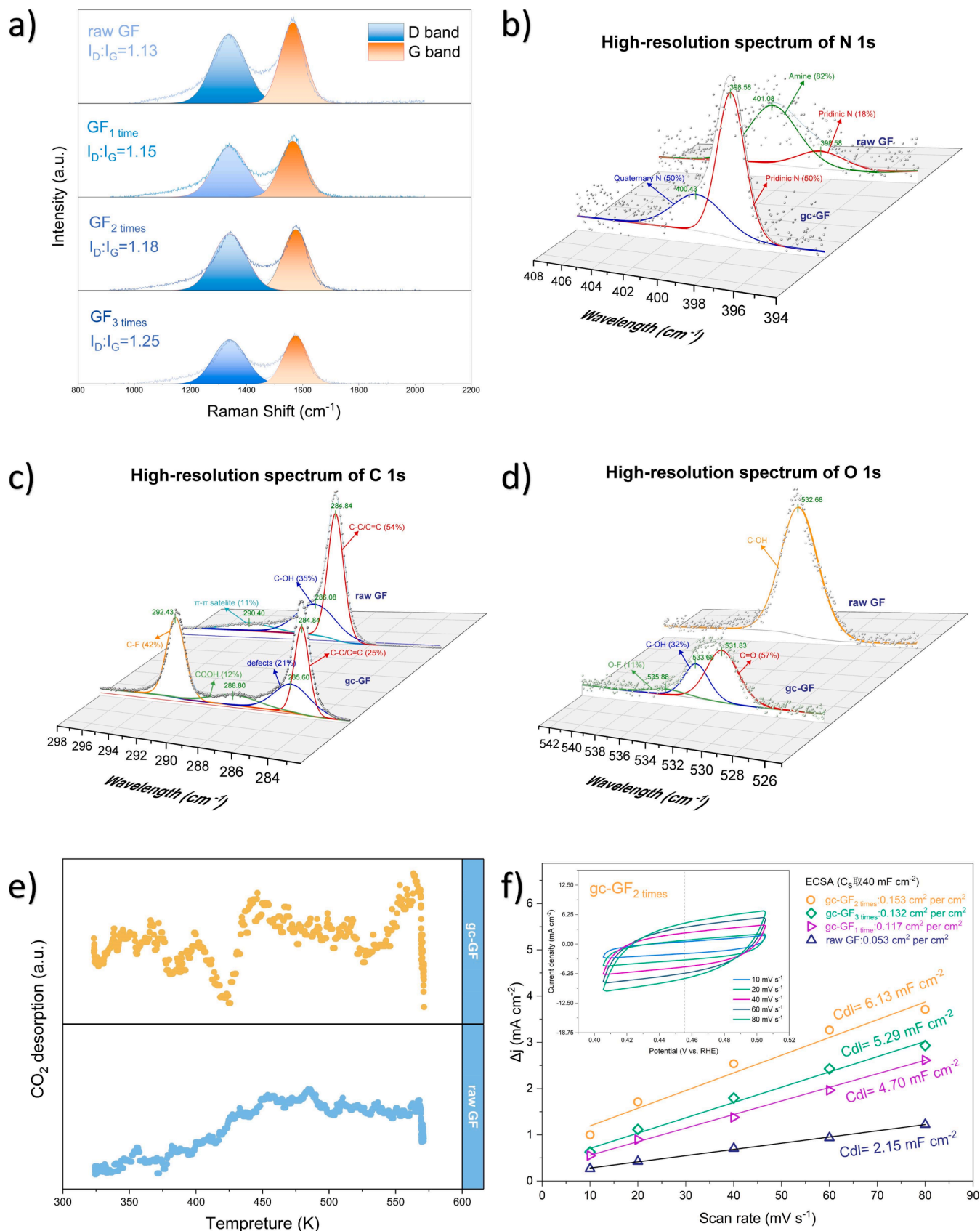


Fig. 2. (a) Raman spectra of different modified GFs; high-resolution spectrum for N 1 s (b), C 1 s (c) and O 1 s (d) from XPS spectrum of gc-GF; (e) (a) CO₂-TPD results for gc-GF and raw GF; (f) ECSA of different GF calculated by capacitance of double-layer method. Inset was CV curves of gc-GF₂ times at different scan rate.

activity, where O_2 molecules were more prone to adsorb on [32]. The carbon atoms adjacent to pyridinic N developed a localized density of states in the occupied region near the Fermi level, suggesting that the carbon atoms could act as Lewis bases due to the possibility of electron pair donation [33]. The adsorption of CO_2 was applied as a probe for Lewis basic sites. Fig. 2e) showed that both gc-GF and raw GF endowed with Lewis basicity with room-temperature adsorbed CO_2 desorbing at high temperatures (450–550 K) on the profiles. This result was associated with the analysis from XPS spectra. It is noteworthy that high Lewis basicity of gc-GF was reflected by emerging two typical Lewis basic peaks centered at 380 K and 420 K. As the initial step of ORR. The emerging graphitic N atom facilitated the charge redistribution by donating an electron to the π -conjugated system, resulting in improved end-on oxygen adsorption on the adjacent α -C atom [34]. Terakura's groups further demonstrated that the hydrogen site, created on pyridinic nitrogen or graphite nitrogen structures during hydrogenation, could be abstracted by approached O_2 molecules to form HO_2 with a lower kinetic barrier in comparison to ordinary O_2 adsorption pathway [35]. The dramatic rise in zeta potential for the mixture of g- C_3N_4 and CNTs as pH decreased below 4 implied that the surface of the prepared electrode was easily protonated (Fig. S8), which may be advantageous in the formation of the special hydrogen site. The large absolute values of zeta potential also implied that a substantial surface charge on the catalysts hampered the aggregation, ensuring the uniform dispersion. Furthermore, the binding energy of *OOH on the structure of pyridinic N or graphitic N was lower than those of other N types, aiding the release of H_2O_2 as a final products [36].

The peaks observed at 284.84 eV, 286.08 eV and 290.13 eV in the high resolution spectra of C were attributed to C-C, C-OH and C-C satellite peak, and upon modification, these were supplanted by four peaks, assigned to C-C (284.84 eV), defects (285.30 eV), $-C=O-O$ (288.48 eV) and C-F (292.43 eV) (Fig. 2c). Notably, The emergence of a defect peak on the gc-GF spectra was corroborated by the increase in I_D/I_G from Raman results. The ratio of C-C peak upon modification decreased from 54 % to 25 %, suggesting the growth of carbon-bearing groups. The spectrum of O apparently indicated that only one peak of raw GF (C-OH, 532.68 eV) increased to three new peaks aligned with $-COOH$ (531.83 eV), $-C=O-O-$ (533.68 eV) and $-O-F$ (535.88 eV) groups on gc-GF after modification (Fig. 2d). The FTIR results provided further evidence of the increase in oxygen functional groups (Fig.S9). The appearance of new oxygen-containing functional groups, as a result of the incorporation of oxidized CNTs, had the capacity to combine with *OOH distinctively [30].

The electrochemical behavior of modified GF with different vacuum filtration-calcination times was evaluated. As illustrated in Fig.S10, gc-GF_{2 times} achieved the highest peak current density of 2.97 mA cm^{-2} and the most positive potential of 0.44 V vs RHE. The incorporation of catalysts significantly enhanced the $2e^-$ ORR performance. High speed charge channels of CNTs directly favored charge transfer in the catalytic layer in spite of the existence of g- C_3N_4 with confined electron transfer ability and insulated PTFE, whose conductivity increased from 1035 to 1118 S/m (Table. S3). Furthermore, there was a sharp decrease of charge transfer resistance of GF after modification (Fig.S11). The electrochemical surface area (ECSA) at the solid-liquid interface is known to be proportional to the capacitance of the double-layer, with calculated C_{dl} values for gc-GF_{1 time}, gc-GF_{2 times}, gc-GF_{3 times} and raw GF being 4.70, 6.13, 5.29 and 2.15 mF cm^2 , respectively (Fig. 2f). The addition of catalysts produced massive active sites on the electrode surface, yet at the third vacuum filtration process, the agglomeration of catalysts stacked to fill existing pores, thus exerting a negative effect. The blockage of the three-dimensional porous structure also inflamed the diffusion of oxygen. The low frequency range of EIS was controlled by the diffusion of reactants. A more gradual slope observed for gc-GF_{3 times} in comparison with gc-GF_{2 times} and gc-GF_{1 time} provided the evidence of the increased obstacle encountered during the diffusion of oxygen in the gc-GF_{3 time} (Fig.S11). Combined with the results of the BET (Table 1), gc-

GF_{2 times} exhibited the highest ECSA (1172.6 cm^2) in comparison to gc-GF_{1 time} (331.4 cm^2), gc-GF_{3 times} (739.0 cm^2) and raw GF (33.7 cm^2).

3.2. The influence of modification on H_2O_2 production

3.2.1. Comparison of different modification on H_2O_2 production

The H_2O_2 production by GFs with different modification was shown in Fig. 3a). All electrodes modified by vacuum filtration displayed a higher H_2O_2 generation rate than that of gc-GF_{impregnation}. After 150 min, the production of H_2O_2 increased from 458 mg/L produced by gc-GF_{impregnation} to 561 mg/L by GF_{1 time}. Vacuum filtration provided a potent driving force and established a dense catalytic layer on the surface of GF (Fig.S3). Partial mixture of electrocatalysts even approached to the other side of GF (Fig.S12). The number of vacuum filtration-calcination cycles had a marked effect on H_2O_2 generation, which following the order of gc-GF_{2times} (709 mg/L) > gc-GF_{3 times} (613 mg/L) > gc-GF_{1 time} (561 mg/L). The highest H_2O_2 concentration of gc-GF_{2times} was attributed to its superior catalytic activity, resulting from an increased loading of electrocatalysts and a well-defined hierarchical porous structure. In light of this, the vacuum filtration-calcination times was chosen as 2 in the electrode fabrication process unless stated otherwise. More details about modification (doping ratio of CNTs to g- C_3N_4 and $2e^-$ ORR electrocatalytic performance of electrodes lacking one doping component) was discussed in the Text. S5.

3.2.2. Influences of PTFE doping amount on GF performance

To gain a comprehensive comprehension of how PTFE influences the catalytic activity of $2e^-$ ORR, the correlation between contact angle, pore distribution, electrochemical impedance spectroscopy (EIS), H_2O_2 production with PTFE doping amount were explored. Except for optimizing carbonaceous by increasing their intrinsic activity and selectivity, high catalytic efficiency from the perspective of liquid/gas wettability on the electrode surface should be considered. Typical amphiphilicity of electrode between hydrophilicity and hydrophobicity was established by regulating the amount of PTFE. The length of polymerized carbon fluorine chain from PTFE was proved to have influence on the hydrophobicity of carbonaceous materials. Therefore, the surface hydrophobicity of GFs with different amount of PTFE doping was investigated through contact angle (CA) measurement (Fig. 3b) and S16). In comparison with the gc-GF_{0 PTFE}, the contact angle apparently increased with increment of PTFE (enlarged from 106° to 156°). Interestingly, when the doping amount increased to 0.1 ml, the interface began to exhibit moderate hydrophobicity ($CA = 121^\circ$), but appeared obvious tendency to hydrophilicity ($CA = 108^\circ$) after a few minutes under the influence of water droplet (Fig.S16 b)). So was the phenomenon of gc-GF_{0 PTFE} (decline from 106° to 95° , Fig.S16 a)). It implies that the interface was not definite waterproof, and the constructed three-phase interface couldn't exist for a long time. Differ from those, the protracted hydrophobicity was basically ensured with further increase of PTFE. Even after 180 min electrolysis (Fig.S17), the CA of gc-GF still maintained at 141° .

As shown in Fig. 3b), the accumulation of H_2O_2 by GF with different doping amount of PTFE displayed a volcano-like trend. The inferior performance of gc-GF_{0 PTFE} (176 mg/L at 180 min) and gc-GF_{0.1 PTFE} (251 mg/L) was due to the ephemeral nature of three-phase interface, which was easily flooded in the electrolyte, thereby leading to narrowing of oxygen transport channel. H_2O_2 accumulation of gc-GF_{0.5 PTFE} accessed to the peak value (725 mg/L at 180 min). Hydrophobic material PTFE favored the establishment of stable gas-liquid-solid three phase interfaces, which thus enabled the direct utilization of both gaseous oxygen from the adhered gas film instead of dissolved oxygen only, largely overcoming the oxygen mass transfer limitation. Nonetheless, H_2O_2 accumulation of gc-GF_{0.7 PTFE} declined to 535 mg/L . This was attributable to the excessive addition of PTFE exacerbated the hydrophobicity of electrode, which prevented the electrolyte from approaching electrode surface, diminishing the tri-phase interface. As a

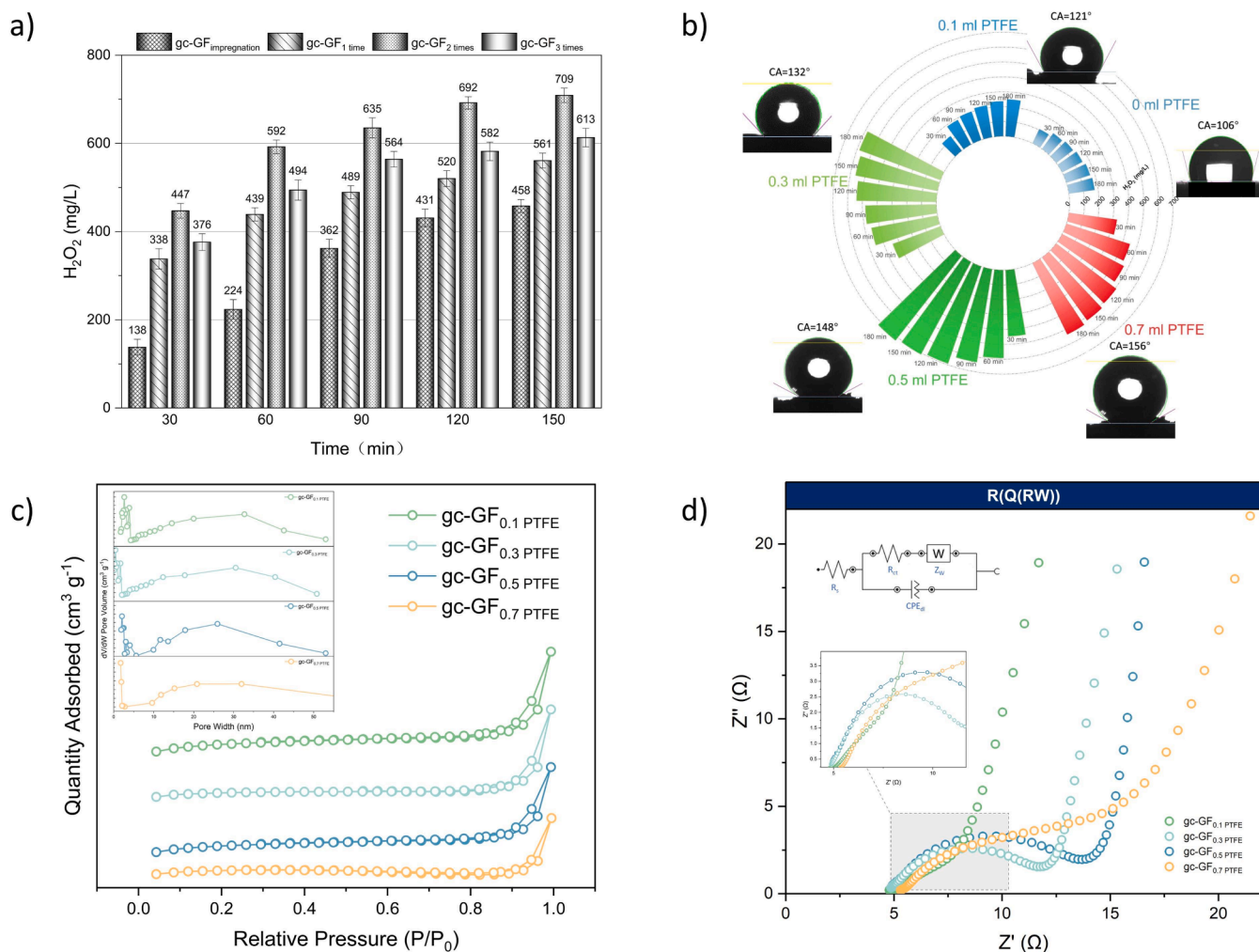


Fig. 3. a) Electrocatalytic 2e⁻ ORR for H₂O₂ production by gc-GF₁ times, gc-GF₂ times, gc-GF₃ times and GF_{impregnation}; b) the effect of PTFE on H₂O₂ accumulation and contact angle of modified GF, H₂O₂ production condition: at the constant current of 0.4 A, initial pH of 9, oxygen aeration rate of 0.7 L/min applied in single-chamber reactor with side-aeration; c) nitrogen adsorption-desorption isotherm of GF with different amount of PTFE doping, the inset was pore distribution of these electrodes; d) Nyquist plots/ fitted curves of modified GF with different doping amount of PTFE.

result, ion transfer became a rate-limiting step in the situation, which decreased ORR efficiency.

To deeply understand the influence of doping PTFE on the structure and porosity, the examination of N₂ adsorption-desorption isotherms was undertaken. As shown in Fig. 3c) and Table 1, electrodes with different PTFE doping maintained basically constant structure of micropores, mesopores and macropores. With the increase of PTFE from 0.1 to 0.7 ml, the BET surface area decreased from 48.32 to 10.12 m² g⁻¹. The volume of total and micropores declined, while the mesopore and macropores swelled. The contracting and agglomeration of PTFE during the sintering process was probably the contributing factor for the phenomenon, which complied with the reported literature [37]. gc-GF_{0.5} PTFE exhibited a preferential pore size within the 10–45 nm range. Mesopore-dominant structure of gc-GF_{0.5} PTFE contributed to the formation of mass transfer channels to facilitate oxygen supply and the release of produced H₂O₂ within a short time. It is salient to bear in mind that the eventual performance of 2e⁻ ORR was contingent on the equilibrium of surface area, active sites, and efficient O₂ transfer from the structure and porosity standpoint. Furthermore, we noted that after coating with more PTFE polymer, the D and G peak of Raman spectra appeared more scattered and wavenumber of FWHM increased about 100 cm⁻¹, which was probably attributed to the cover of carbonaceous signature by the increase of doped PTFE (Fig.S18 and Table S4).

As show in Fig. 3d) and Table S5, the R_s was basically kept in the

range of 4.78–5.30 Ω, predominantly determined by the resistance of the electrolyte between the reference electrode and the working electrode. As the quantity of PTFE increased, the R_{ct} increased incrementally from 5.15 to 12.57 Ω. The augmentation of the R_{ct} was attributed to the impeded ion transition between the more hydrophobic electrode surface and electrolyte caused by the non-conductive PTFE doping. In the low frequency, the mass transfer resistance decreased from 21.3 to 16.2 mΩho*s^(1/2) as PTFE amount increased from 0.1 to 0.5 ml. However, excessive PTFE doping played a limit on ion transmission (25.4 mΩho*s^(1/2)) for gc-GF_{0.7} PTFE, which was owing to the superhydrophobic electrode surface obstructed H⁺ transfer from electrolyte and diminished the three-phase reaction sites.

3.3. The promotion of H₂O₂ production by side-aeration

Extensive studies have been conducted to improve the catalytic activity of electrodes, as opposed to the low oxygen utilization efficiency and mass transfer of O₂, both of which impede the scalability. As depicted in Fig. 4a), gaseous oxygen initially dissolves in the electrolyte to form dissolved oxygen (O₂, bulk), subsequently diffusing from bulk to the compact layer, traversing diffusion, and diffuse layer. The ORR then occurs in terms of an inner-sphere reaction on the inner Helmholtz plane (IHP) or an outer-sphere reaction on the outer Helmholtz plane (OHP). In general, mass transfer of O₂, bulk in the diffuse layer could be

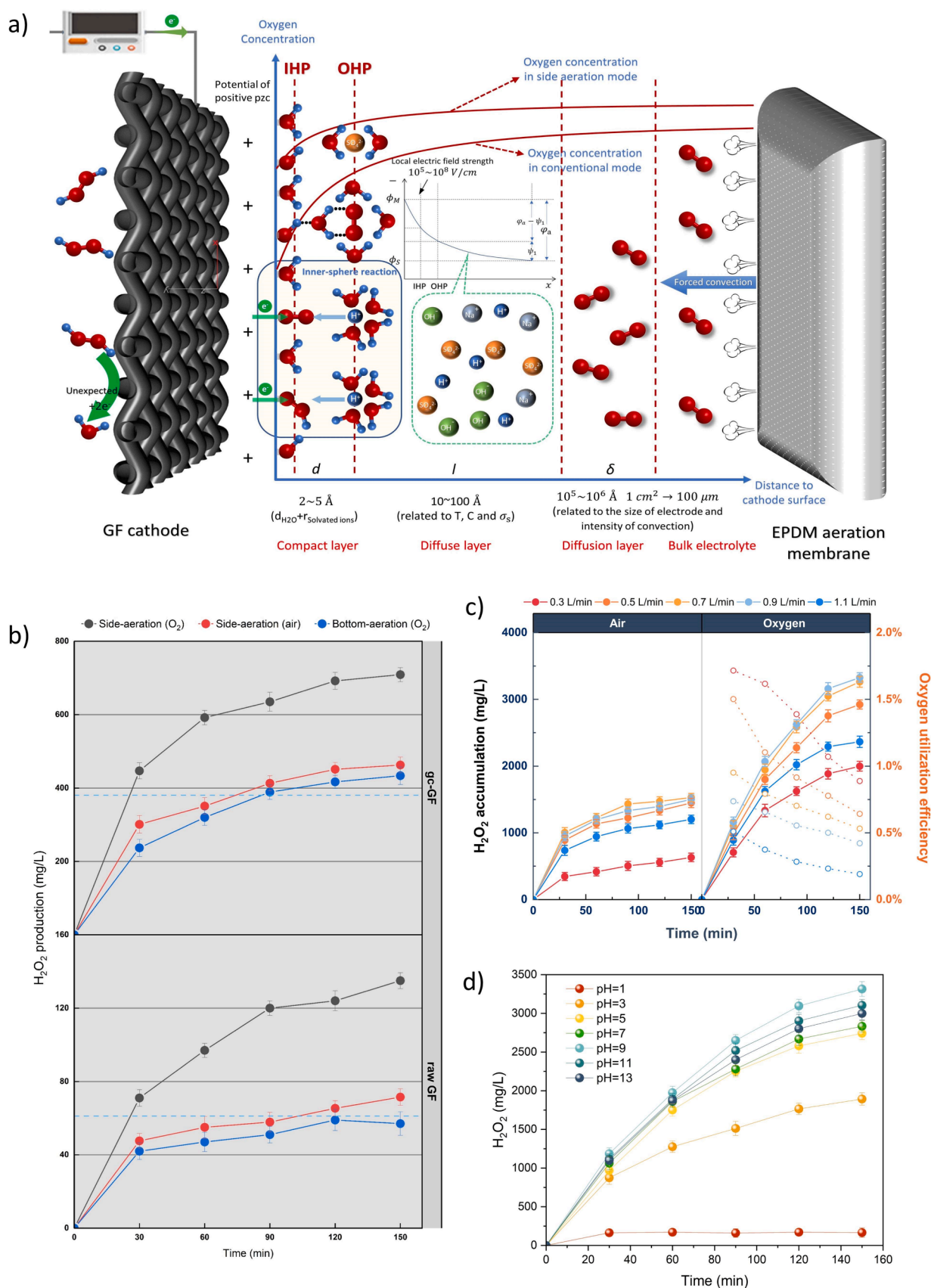


Fig. 4. a) O_2 diffusion scheme of side-aeration; b) H_2O_2 production with different aeration mode, condition: constant current= 0.4 A, initial pH= 9, gas flow rate= 0.9 L/min in the single-chamber with side aeration; Effect of c) aeration rate (the solid circle represented the amount of H_2O_2 accumulation and the hollow circle represented the oxygen utilization efficiency) and d) initial pH on H_2O_2 production. Conditions: except for investigated factor, the other parameters were set at electrode gap of 1.8 cm, constant current of 0.4 A, oxygen aeration rate of 0.9 L/min and initial pH of 9 in the dual-chamber compartment with side aeration.

neglected, since the diffuse layer is consequent of thermal ionic charge movement, and the thickness of the diffuse layer is approximately 10^{-4} -fold of the diffusion layer. The ordinary SAE is typically unable to replenish continuous consumption of $O_{2, \text{bulk}}$ in the vicinity of cathode via ORR at large current density because of mass transfer resistance in diffusion layer and low initial dissolved oxygen, thus aggravating the side aeration and energy consumption from concentration polarization of O_2 . In the proposed side-aeration configuration, continuously external supply of O_2 provided forced convective transport prior to the diffusive transport, regulating the thickness of diffusion layer, and augmenting the concentration gradient of oxygen. Gas flow through graphite felt favored the timely departure of as-generated H_2O_2 from electrode surface, avoiding the deep pathway of $4e^-$ ORR. The interception of crosslinked GF also lengthened the residence time of air bubbles in the electrolyte.

As illustrated in Fig. 4b), it is evident that the cumulative H_2O_2 of raw GF and gc-GF under O_2 aeration were limited to 43 mg/L and 422 mg/L in the bottom aeration (aeration was supplied by a pump strip on the bottom of the reactor). Fortunately, the same measurements of cumulative H_2O_2 were raised to 134 mg/L and 709 mg/L when side aeration was employed, thus exhibiting the effect of side-aeration in augmenting cathodic H_2O_2 production. By applying pressure to the EPDM membrane, the size of produced bubbles was reduced compared to that of bottom aeration. This reduction in bubble size was beneficial to increasing the pressure gap between the liquid-gas interface (in accordance with Yong's equation, Eq. 6 and Eq. 7) [38], thus accelerating the exchange of oxygen at the bubble interface, ultimately resulting in a higher concentration of dissolved oxygen (17.8 mg/L with O_2 aeration and 7.3 mg/L with air aeration) in a shorter time (75 s with air aeration) as depicted in Fig.S19). Simultaneously, the oxygen mass-transfer efficiency (KLa) also increased from 0.0089 (air) and 0.0137 (oxygen) with bottom aeration to 0.0102 (air) and 0.0167 (oxygen) with side aeration (Fig.S20)). Furthermore, a slight increase of H_2O_2 production was observed when side aeration by air substituted for bottom aeration by O_2 , while the DO in the former was lower than the later, it is extrapolated that the improvement on gas diffusion path played a more important role than that of initial concentration of O_2 in this configuration for H_2O_2 production.

$$\Delta P = \frac{2\sigma}{\gamma} \quad (6)$$

$$A = \frac{3V}{\gamma} \quad (7)$$

Where ΔP is the pressure difference between inside and outside of the bubble, σ is the surface tension and γ is the ratio of bubble, A is the surface area of the bubble, V is the volume of bubble.

3.4. Variables of electrocatalytic $2e^-$ ORR

3.4.1. Effect of dual-chamber configuration on H_2O_2 production

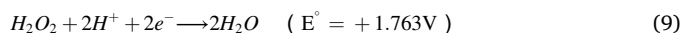
The dual-chamber configuration is another reactor option to improve H_2O_2 accumulation, which is effective for transportation of protons liberated at the anode and avoids the anodic oxidation of H_2O_2 formed at the cathode. As shown in Fig.S21, H_2O_2 accumulation rose to more than 2000 mg/L in the dual-compartment cell, along with a discernible rise in current efficiency and a reduction in energy consumption. Due to the difference on the construction of undivided cell and dual-chamber reactor, the effect of electrode spacing was discussed. The greatest H_2O_2 production was obtained at the inter-electrode gap of 1.8 cm (3314 mg/L). The energy consumption increased from 35 to 50 kWh/kg H_2O_2 and the current efficiency decreased from 48 % to 35 % with the enlargement of plate distance from 1.8 cm to 2.8 cm. Narrower spacing lead to higher mass transfer and provided a smaller ohmic drop in the catholyte. However, the electrode spacing must not be too close to the

PEM, as this would impede continue proton exchange and long-term utilization.

3.4.2. Effect of constant current on H_2O_2 production

The quantitative effect of constant current on the electrocatalytic H_2O_2 production was elucidated at fixed values of 0.1 A, 0.2 A, 0.4 A, 0.6 A and 0.8 A. As illustrated in Fig.S22, the H_2O_2 yields exhibited distinct volcano trend. Increase on H_2O_2 production was observed as current increased from 0.1 A (2281 mg/L within 150 min) to 0.4 A (3314 mg/L within 150 min). It can be attributed to the influence of potential on the Fermi level of the electrode, which altered the chemical potential of electrons ($\Delta G = neU, \mu_e$) [39]. Negative shift of potential lowered the reaction activation energy ($\Delta G^\ddagger - a\eta F$), accompanied with the increase of reaction rate (k) according to the Eyring-Polanyi equation (Eq. 8) [40]. Nevertheless, the generation of H_2O_2 decreased accompanied with the further increase of constant current, which declined to 2996 mg/L at 0.6 A and 1759 mg/L at 0.8 A. The deterioration of H_2O_2 yield was mainly attributed to the intensified thermodynamic driving force of competing reactions such as the reduction of H_2O_2 to H_2O (Eq. 9), hydrogen evolution (Eq. 10) and oxidation of H_2O_2 at the anode (Eq. 11)). And to the aspect of alteration on adsorption energetics, negative shift of potential perturbed the bond strength of reactants, intermediates or products towards the electrode surface through changing the Frontline orbital energy of the electrode (Fig.S23) [41]. The increased overpotential enlarged the bond strength of a series of intermediates towards electrode surface ($*O_2$, $*OOH$), resulting in the breaking of O-O bond and formation of rather stable interacting $*O \cdots *OH$ pairs after first PCET step or during second PCET process (Eq. 12), which led to the formation of a water molecule and an $*O$ intermediate). The thin film arising by these adsorbed oxygenated species blocked the bridge sites for the Langmuir adsorption of O_2 , at least for some time, reducing the possibility for an effective ORR. Although the elevated temperature (T) by electrothermal effect ($1 \text{ mV} \cdot F \approx 100 \text{ J/mol}$, Fig.S24) accelerated the kinetic rate (k) of reaction (Eq. 8), the solubility of saturated DO decreased 1.46 mg/L from 24 °C to 36 °C and H_2O_2 is unstable with respect to the disproportionation of H_2O_2 into O_2 and H_2O at high temperature (generally exacerbated 2.5 times per 10 °C), which overshadowed the improvement of kinetic rate [42]. The optimal current density of 33.3 mA cm^{-2} (0.4 A) achieved in this study surpassed the conventional ranges observed in submerged and aerated electrodes (approximately $0.4\text{--}1.5 \text{ mA cm}^{-2}$). This notable disparity strongly suggests that the combination of gc-GF with side aeration push the electrosynthesis of H_2O_2 towards actual environmental application a big step.

$$k = Ae^{-\frac{\Delta G^\ddagger}{RT}} e^{\frac{a\eta F}{RT}} (\eta = |\varphi - \varphi^0|) \quad (8)$$



3.4.3. Effect of gas flux on H_2O_2 production

DO concentration is a key parameter for the ORR efficiency. As discussed above, the DO concentration with pure oxygen sparged was more than two times as that of air aeration, which brought about a remarkable increase of H_2O_2 from the highest production of 1530 mg/L with air aeration to 3314 mg/L aerated by pure oxygen (Fig. 4c)). The H_2O_2 accumulation with different oxygen aeration rate followed the order of 0.9 L/min (3314 mg/L), 0.7 L/min (3062 mg/L), 0.5 L/min (2923 mg/L), 1.1 L/min (2365 mg/L) and 0.3 L/min (1999 mg/L), accompanying by an exceptional oxygen utilization efficiency range (0.5–1.7 %). Higher aeration rate supplied sufficient oxygen to the

electrolyte, thus promoting ORR with less side reactions and reducing the concentration overpotential. Considering the formation process of gas bubbles, a higher gas flow rate induced faster water flow velocity (v) and altered the pressure variance between two sides of the bubble (P), providing impetus to the formation of more gas bubbles according to the Bernoulli equation (Eq.13) [43]. Additionally, the high gas flux rate enabled the departure of in-situ generated H_2O_2 from the cathode margin to the bulk, averting the ongoing reduction of H_2O_2 . There was no obvious difference in H_2O_2 production with air aeration rate from 0.5 to 0.9 L/min, which might be ascribed to the proximity of saturated O_2 in the electrolyte. However, as the aeration rate reached 1.1 L/min, the strong impact force of air flux caused an inadequate contact between bubbles and electrode, thus leading to the decrease of three-phase interface.

$$P + \frac{1}{2}\rho v^2 = C(\text{constant}) \quad (13)$$

Where ρ is the liquid density.

3.4.4. Effect of initial pH on H_2O_2 production

Evidently, pH had a pronounced impact on the H_2O_2 production shown in Fig. 4d). At the initial pH of 9, the gc-GF displayed the highest H_2O_2 production of 3314 mg/L, which is 20.08, 1.75, 1.21, 1.17, 1.07, 1.10 times higher than those in pH= 1, 3, 5, 7, 11, 13, respectively. To shed more light on the effect of electrolyte pH, the CV experiments were performed in alkaline (0.1 M KOH, pH=13), neutral (0.1 M Na_2SO_4 , pH=7) and acidic (0.1 M $HClO_4$, pH=1) electrolyte (Fig. 5a)). No conspicuous ORR peak was observed in acidic media corresponding to the inferior performance on H_2O_2 production. The most favorable potential was obtained by operating at pH 13.0, with an onset potential of 0.48 V vs RHE. Approximate 90 mV lower overpotential was clearly reflected in alkaline media over the entire kinetic-diffusion region compared to the neutral counterparts. This phenomenon was in accordance with the so-called kinetic affinity of ORR in alkaline media. Given the pH-independence of $O_2/\cdot O_2^-$, the standard potential of this reaction ($E^\circ = -0.3 \pm 0.03$ V vs SHE) didn't change with the variation of pH. However, the standard potential for whole ORR process (the reduction of O_2 to H_2O/OH^-) decreased when pH traversed from 0 to 14 (Fig.S25). The overpotential for the first electron transfer step ($O_2/\cdot O_2^-$) exhibited a

sharp decrease at alkaline pH (1.53 V at pH=0–0.7 V at pH=14), which was the primary thermodynamic reason for the better electrocatalytic activity of a broad array of carbonaceous materials in alkaline media. Tafel plots were obtained to gain a deeper understanding of ORR mechanism, which was depicted in Fig.S26 and Table S6. In comparison to the condition of neutral media, gc-GF achieved a lower Tafel slope (174 mV dec^{-1}), a higher exchange current density (8.37 nA cm^{-2}) and transfer coefficient (0.337) in the alkaline electrolyte. These results suggested that in the alkaline condition, the requirement for overpotential to derive net current is lower (lower b); the necessity of active energy for electrochemical reaction was reduced and the reaction rate was more rapid at the equilibrium state (higher j_0); a higher proportion of Gibbs free energy was devoted to transforming the positive direction of oxygen reduction process (higher α).

To further explore the selectivity of gc-GF towards $2e^-$ ORR, RRDE measurement was conducted with fixed potential at ring electrode so that only H_2O_2 oxidation current was detected. As illustrated in Fig. 5b), gc-GF showed the highest overall catalytic reactivity for oxygen reduction (disk current up to 1910 μA at 0 V_{RHE}) and largest H_2O_2 specific productivity (ring current up to 118 μA at 0 V_{RHE}) in the alkaline electrolyte, and the onset potential was near the thermodynamic equilibrium potential of 0.695 V_{RHE} , corroborating the low overpotential for alkaline ORR mentioned above. At the potential range of 0–0.3 V, the calculated electron transfer number was 2.56–2.60, which was associated with a high H_2O_2 selectivity of 70–72 % and demonstrated the dominance of $2e^-$ ORR over the applied potential window. The moderately high H_2O_2 selectivity kept stable in alkaline electrolyte, while more obvious potential-dependence with wider span in selectivity was observed in neutral (59–69 %) and acidic (29–45 %) electrolyte. The selectivity and electron transfer number were double-checked by preparing Koutecky-Levic (KL) plots derived from RDE voltammetry (Fig. S27). As shown in Fig. 5c), the linearity of KL plots indicated a first-order reaction toward dissolved oxygen at each set pH. The values of n at 0 V vs RHE were 2.60, 2.63 and 3.11 at pH= 13, 7, 1, respectively. Table 2 displayed a comparison of selectivity towards H_2O_2 determined by RRDE voltammetry and KL plots, where both results exhibited good conformity. Above findings collectively manifested the alkaline preference of on-site H_2O_2 production in the system.

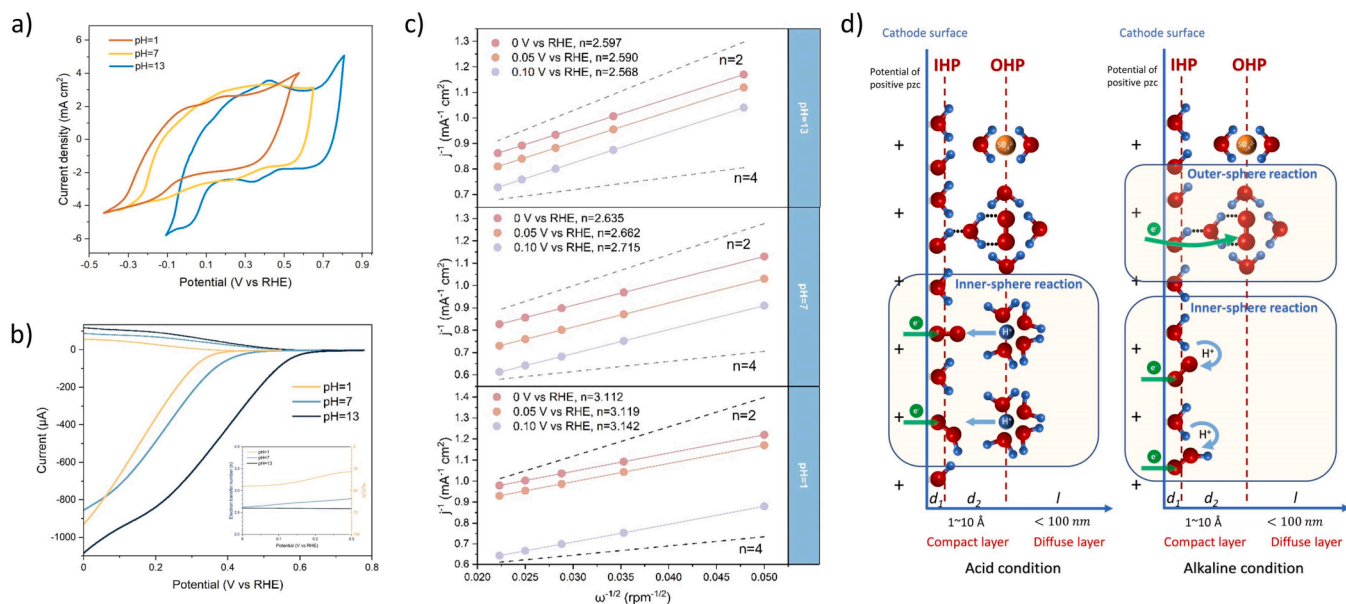


Fig. 5. a) electrochemical analysis of O_2 reduction through cyclic voltammetry at different pH; b) Rotating ring-disk electrode measurements with a rotation speed of 1600 rpm and a sweep rate of 10 mV s^{-1} , inset was the calculated electron transfer number (n) and H_2O_2 selectivity for gc-GF; c) KL plots for gc-GF; d) schematic illustration of the double-layer structure during ORR in acidic (left) and alkaline (right) conditions.

Table 2

Selectivity toward two-electron reduction and electron transfer number evaluated from RRDE voltammetry and Koutecky-Levic (KL) Plots.

	Selectivity (Electron transfer number)								
	pH= 1			pH= 7			pH= 13		
resource	0 V	0.05 V	0.1 V	0 V	0.05 V	0.1 V	0 V	0.05 V	0.1 V
RRDE	45.5% (3.09)	44.5% (3.11)	43.0% (3.14)	69.0% (2.62)	67.5% (2.65)	65.0% (2.70)	69.5% (2.61)	70.2% (2.60)	70.5% (2.59)
KL plot	44.4% (3.11)	44.4% (3.12)	42.9% (3.14)	68.3% (2.63)	66.9% (2.66)	64.3% (2.72)	70.2% (2.60)	70.5% (2.59)	71.6% (2.57)

3.5. Discussion on demonstrated preference of 2e⁻ ORR in alkaline condition

Transitioning from acidic to alkaline environment played several effects on the electrochemical interface in terms of double layer structure, adsorption strength of oxygenated species and working electrode potential range. Indeed, ORR, multielectron transfer process, was undoubtedly classified as an inner-sphere electron transfer reaction, while there was a surface-independent outer-sphere electron transfer pathway in the overall 4e⁻ ORR, which was found to predominantly promote a 2e⁻ reaction pathway to HO₂⁻ anion as a final product in alkaline condition.

As depicted in Fig. 5d) for typical O₂-saturated alkaline condition, the cluster of O₂·(H₂O)_n weakly interacted with the surface species (OH_{ads}) via a hydrogen bond between H atom in OH_{ads} and O atom in solvated molecular O₂. The formation of the hydrogen bond played a role in stabilizing the O₂·(H₂O) cluster in the OHP. Meanwhile, profited by the decrease of overpotential for O₂ reduction to O₂⁻ in alkaline media, finite hydrogen bond energy (<35 kJ mol⁻¹) is sufficient enough to overcome the overpotential and promotes an outer-sphere electron transfer to form-O₂⁻ [3]. Specifically, this outer-sphere reaction mechanism was only existed on the electroneutral hydroxyl species region and depends on the extent of OH_{ads} coverage, which could be easily derived from the complete discharging electron of abundant hydroxyl anion (OH⁻) on the electrode surface provided by alkaline media [44]. The explicit process of outer-sphere electron transfer was depicted in Text S6. Hence, the hydroxyl species (OH_{ads}) no longer only played an inhibiting effect of site-blocking for ORR in the alkaline condition, but serve as an outer-sphere bridge between the reactant and electrode surface [45]. An intriguing finding arose from the observation in the double-layer capacitance across varying pH range (Fig.S28). Concomitant with an elevation in pH, there emerged a downward trend in the C_{dl}, so was the ECSA. In alkaline environments, the reduction in ECSA can be ascribed to the occupation of active sites by anionic species, especially hydroxide ions. Despite the decrease in ECSA, the 2e⁻ ORR within gc-GF showed a pronounced preference for alkaline conditions, thereby highlighting the influence of outer-sphere bridging facilitated by adsorbed hydroxyl species in the alkaline media, from an alternative perspective. Furthermore, the binding energy of (·HO₂)_{ads} on the surface hydroxyl species of electrode was likely lower than those of hydroxyl species-free sites, giving rise to the desorption of ·HO₂⁻ anion into the electrolyte. In the meanwhile, the carbon substrate also supported this outer-sphere electron transfer via mediation by the quinone/hydroquinone surface functional groups [46], whose existence was identified by the obvious peak at 1719 cm⁻¹ on the spectra of FTIR. The explicit scheme of outer-sphere electron transfer mechanism was depicted in Text S5. On the contrary, in acidic media, though the formation of hydrogen bond was still in existence, the interaction energy was not enough to allow electron transfer to solvated molecular O₂ compared with high overpotential in acidic media [3]. The OH_{ads} coverage from water activation primarily inhibited the adsorption site of O₂ and other intermediates in the acidic electrolyte, obstructing the production of H₂O₂.

The alteration of pH also had the potential to change the properties of the electric double layer at the electrode/electrolyte interface, such as the surface charge density, resulting in a difference of the adsorptive strength for oxygenated species. The alteration in C_{dl} at different pH served as evidence supporting the occurrence of changes in the double layer structure (Fig.S28). The potential of zero charge (PZC) for

carbonaceous materials was extremely negative aligning with the relatively low work function of these materials ($\Phi_{\text{carbonaceous materials}}=4.3\text{--}5.3\text{ eV}$, $\Phi_{\text{CNTs}}=4.4\text{ eV}$, $\Phi_{\text{g-C}_3\text{N}_4}=4.76\text{ eV}$, $\Phi_{\text{P}}=5.6\text{ eV}$) [47]. As ions in the electrolyte underwent significant changes with pH from 0 to 14, there was approximately 0.8 voltage positive shift of PZC for the carbonaceous material. In acidic condition, high density of positive charge accumulated on the electrochemical interface, bringing about the strong adsorption of the oxygenated species. The powerful adsorption exacerbated the cleave of O-O bond, which promoted the ORR towards 4e⁻ pathway. On the other hand, the decrease of positive charges in alkaline media would likely facilitate the binding capability to locate in an appropriate state. This effect brought by pH-disparity played a slight effect on the noble-metal materials containing relatively positive PZC, such as Pt electrode.

A chemical reaction was generally determined by both kinetics and thermodynamics. For the pH-dependence of whole ORR process, the thermodynamical aspect was associated with the reaction potential. Due to the decrease of standard potential from 1.229 to 0.401 V_{SHE} in traversing pH from 0 to 14, the working potential range negatively shifted about 0.83 V. The lower working electrode potential in alkaline condition brought about more negative charge accumulated on the electrode surface, which repelled the produced HO₂⁻ away from inner-Helmholtz to the electrolyte. Analogically, the poison effect from negative halide anions were alleviated. Reversely, in acidic media, more positive charge decreased the possibility of H₂O₂ desorption from the electrode surface [48].

Essentially, the activity and selectivity of modified electrode at various pH was contingent upon the nature of electrode, which eventually determined the interaction between reactants and electrode. It has been reported that electronic modification introduced by high content of nitrogen doping were sensitive to the pH condition, which played a vital or even decisive role in ORR activity. The reported carbonaceous material with more than 10 at% nitrogen doping exhibited inactive under low-pH condition, which corresponded to the results of gc-GF (13.82 at % nitrogen in Table S2). Simultaneously, alkaline media essentially acted as a homogeneous catalyst to intrigue the stability of HO₂⁻ in alkaline media but not in acidic media [49].

Moreover, solvation effect brought by electrochemical environmental variability also affected the ORR process. As elucidated in Marcus Theory (Eqs. 14 and 15), solvation shell was closely related to the electrochemical environment and recombination energy (λ) directly affected the activation energy of reaction [50]. The fluctuation of environmental (solvent) energy is the driving force behind the crossover of the reaction barrier (Eq. 16) [51]. The reaction process was also limited by solution viscosity, which was demonstrated by Kramers Theory (Eq.17) and Einstein-Stokes formula (Eq. 18, D: transfer coefficient, η : solution viscosity) [52]. Higher pH aggravated the lower O₂ solubility (C_{O_2}), lower diffusion coefficient (D_{O_2}) and higher kinematic viscosity (ν), which was one of reasons for the decrease of H₂O₂ production in going from pH = 9–13 [53]. It was also reported that ORR polarization curves of same electrocatalysts exhibited a lower diffusion limited current density in 1.0 M NaOH compared to that in 0.1 M NaOH [3]. In the meanwhile, the necessity of proton for PCET process in the case of high pH environment was provided by the co-adsorbed water on the electrode surface or the partial water shell of ions (Fig. 5d)) [54]. Increasing the alkalinity of supporting electrolyte (pH>9), the water activity would gradually decrease, which jeopardized the proton

transfer for ORR.

$$\Delta G^\ddagger = \frac{(\lambda - \eta F)^2}{4\lambda} \quad (14)$$

$$\lambda = \lambda_0 + \lambda_i \quad (15)$$

$$k = \frac{\Delta \varepsilon}{\hbar} e^{\left(-\frac{\Delta G^\ddagger}{RT}\right)} \quad (16)$$

$$k = \frac{\omega_R \omega_B m}{2\pi \gamma} \quad (17)$$

$$\gamma = \frac{k_B T}{D} = 6\pi \eta r \quad (18)$$

3.6. Stability test, performance comparison and application in electro-Fenton

The stability of modified electrode on H_2O_2 production was an essential factor from practical application. To inspect the stability of the proposed coupling system, gc-GF was consecutively conducted in the dual-chamber configuration with side-aeration for 10-times. As illustrated in Fig.S29, H_2O_2 yield still maintained 3014 mg/L with maximum decrease no more than 6.6 %. The slight decline of H_2O_2 production was probably ascribed to the bowing or partial delamination of catalytic layer encompassed consecutive cycles. Despite scanning 400 cycles of CV, the activity of gc-GF was negligible loss in terms of onset potential,

reduction peak and capacitance current. Additionally, the chronoamperometric response of gc-GF kept generally stable, which both indicated the stability of GF after modification (Fig. 6a)). The long-chain polymeric PTFE and impetus from vacuum filtration during modification effectively immobilized the solid catalysts on the carbonaceous scaffold during long-term operation, inhibiting the catalysts to drop off the electrode. The concise structure of side-aeration also avoided the drawbacks of typical GDE, which would be rapidly damaged without injecting O_2 .

Compared with other literatures, the side-aeration configuration coupling with gc-GF exhibited obvious advantages in terms of H_2O_2 generation ability, oxygen utilization efficiency and stability. As depicted in Fig. 6b) and Table 3, H_2O_2 generation ability of GF modified by various types of methods (anodization [31,55], doping electrocatalysts [58,61], chemical surface modification [56,57,60]) centered in the range of 1–2 $\text{mg h}^{-1} \text{cm}^{-2}$. When the gc-GF combined with the configuration of side-aeration, the H_2O_2 yield capacity and oxygen utilization efficiency remarkably enhanced to 4.44–6.89 $\text{mg h}^{-1} \text{cm}^{-2}$ and 0.66–1.62 %, which was even advantageous to partial typical GDE [62, 63] and simple aeration promotion inserting the piping into the interior of electrode to aerate [65]. Superior reusability of the proposed system promised it equally attractive for on-site H_2O_2 production in practical application.

Finally, based on electrochemical on-site production of H_2O_2 , a range of typical organic contaminants (TC, BPA, phenol and 2,4-D) were selected as target pollutant to explore the potential of this system in

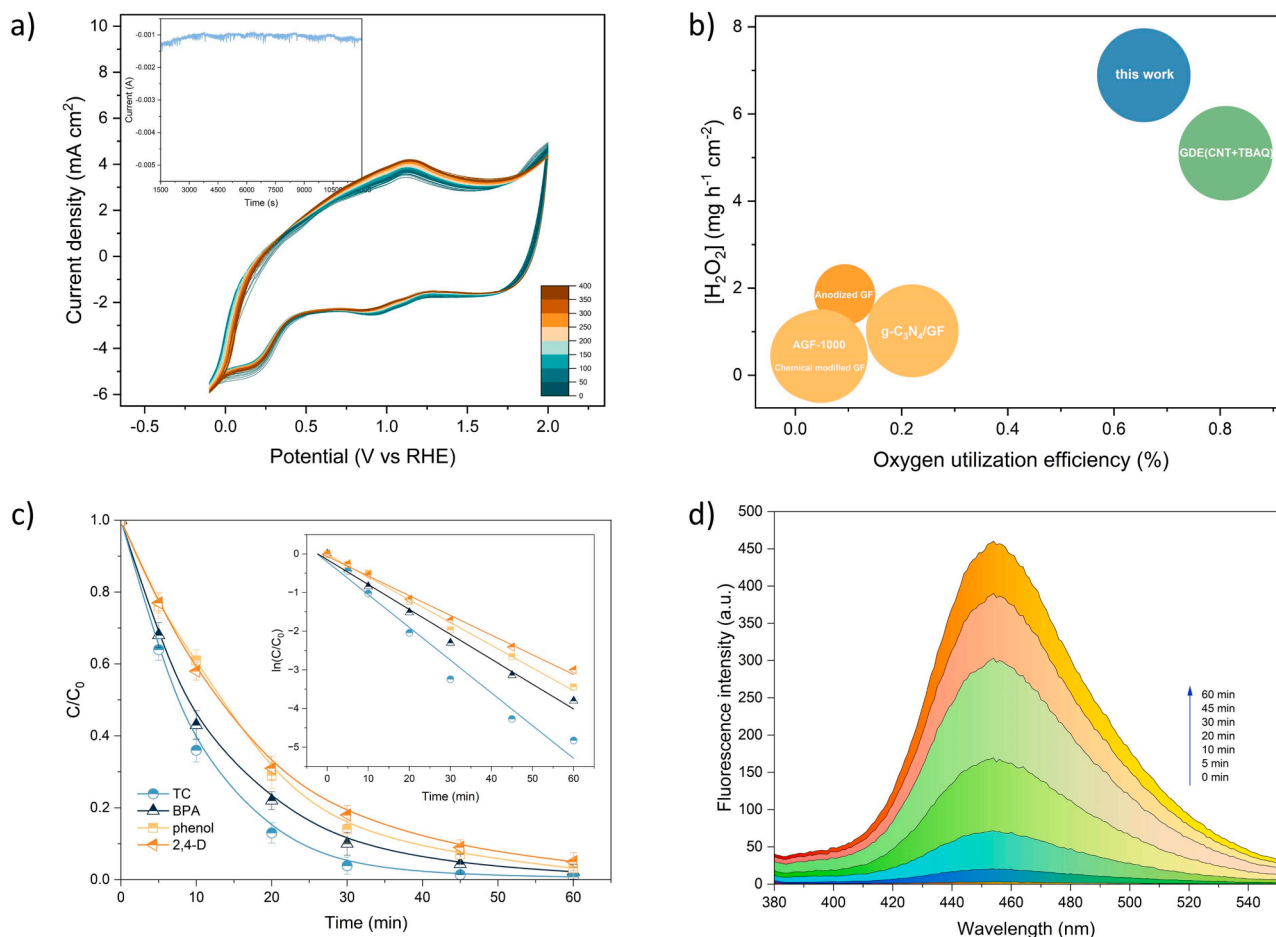


Fig. 6. a) Cyclic Voltammetry for gc-GF within consecutive scan of 400 times. The inset was Chronoamperometric response of gc-GF in O_2 saturated solution; b) comparison of this work with other reported literatures on H_2O_2 generation ability, oxygen utilization efficiency and stability. Note: the radius of circle represents the stability of electrode after 5 runs; d) degradation of different target pollutants. Inset was the corresponding kinetic rate of degradation; d) Fluorescence spectra of 7-hydroxycoumarin within reaction time.

Table 3Comparison of H₂O₂ electro-generation with other literatures.

Cathode	Experimental conditions				[H ₂ O ₂] (mg h ⁻¹ cm ⁻²)	Oxygen utilization rate (%)	Stability (% after 5 cycles)	Reference
	pH	Current density or applied potential	t (h)	O ₂ flux rate (L/min)				
Anodized GF	6.4	-0.65 V (vs SCE)	2	0.4	1.56	0.047	-	[55]
Anodized GF	0.7	-0.60 V (vs SCE)	2	0.4	1.85	0.093	62.4	[31]
Chemical modified GF	-	-0.65 V (vs SCE)	2	0.4	1.14	0.034	-	[56]
Surface modified GF	3	0 V (vs RHE)	2	0.08	2.13	0.088	-	[57]
g-C ₃ N ₄ /GF	3	12 mA cm ⁻²	1	0.36	1.02	0.22	94.9	[58]
CNT/PTFE/GF	3	132	5	0.14	0.11	0.007	-	[59]
AGF-1000	13	-0.65 V (vs SCE)	1	0.6	0.44	0.037	91.6	[60]
GF	6.4	-0.65 V (vs SCE)	2	0.4	0.44	0.048	95.6	[61]
GDE	3	20 A m ⁻²	3	0.33	1.04	0.089	-	[62]
GDE	3	204 A m ⁻²	5	0.14	1.94	0.082	-	[63]
GDE(CNT+TBAQ)	3	10.7 mA cm ⁻²	2	0.4	5.10	0.81	96.7	[64]
GF-inside aeration	6.4	88.2	1	0.6	1.94	0.159	-	[65]
gc-GF	9	6.7 mA cm ⁻²	1	0.3	4.44	1.617	-	This work
	9	6.7 mA cm ⁻²	1	0.7	6.48	0.703	-	
	9	6.7 mA cm ⁻²	1	0.9	6.89	0.656	96.2	

environmental remediation through electro-Fenton (EF) process. Although the initial concentration of selected pollutants stated at a high value (100 mg/L), TC (99.2 %), BPA (97.7 %), phenol (96.8 %) and 2,4-D (94.9 %) were virtually eliminated in 60 min with a kinetic rate of 0.0847, 0.0643, 0.0587 and 0.0509 min⁻¹ (Fig. 6c)). Briefly, the bulk H₂O₂ was continuously produced by the modified cathode with side aeration and then reacted with Fenton catalysts to generate powerful oxidant of hydroxyl radicals. Therefore, capture experiments of hydroxyl radicals were carried out by ESR (instantaneous production of ·OH) and photoluminescence method using coumarin as prob (cumulative amount of ·OH). The 4-fold peaks of DMPO-·OH adducts with an intensity ratio of 1:2:2:1 obviously emerged by ESR experiment and a typical characteristic peak of 7-hydroxycoumarin (adduct of coumarin and ·OH, E_m/E_x = 455/332 nm) were observed, which showed an apparent increase with prolonged reaction time (Figs. S30 and 6d)). Both results authenticated the substantial production of ·OH by the constructed configuration through EF process. Profited from a multitude of generated hydroxyl radicals, 61 %, 64 %, 53 % and 48 % of TC, BPA, phenol, and 2,4-D were thoroughly mineralized within 2 h in the fabricated apparatus (Fig.S31), thereby further demonstrating the adaptability of this on-site H₂O₂ production configuration for the EF application.

4. Conclusion

In this study, g-C₃N₄, CNTs and PTFE were doped on the GF substrate through vacuum filtration-calcination process, which enhanced H₂O₂ production from 134 mg/L by raw GF to 709 mg/L within 150 min. A series of physiochemical and electrochemical measurements was conducted to gain an insight into the correlation of electrocatalysts, vacuum filtration-calcination times and doping amount of PTFE with electrocatalytic performance towards 2e⁻ ORR. A multitude of N-functional sites (pyridinic nitrogen and graphitic nitrogen) brought by g-C₃N₄ prevented the cleavage of O-O bond during ORR process. CNTs facilitated the charge transfer in the catalytic layer despite the existence of g-C₃N₄ with confined charge transfer ability and insulated PTFE. The well-constructed mesopore structure and three-phase interface improved the mass transfer of oxygen. To address the problem of inferior oxygen mass transfer in the ordinary device, a side aeration configuration was proposed, which reduced the thickness of diffusion layer and favored the departure of as-generated H₂O₂. The oxygen mass-transfer efficiency and H₂O₂ production increased from 0.0137 and 422 mg/L by bottom aeration to 0.0167 and 709 mg/L in the undivided reactor with side aeration. It is noteworthy that the convenient combination of side aeration and modified GF in the dual-chamber configuration rendered a

qualitative leap of H₂O₂ generation capacity to 4.44–6.89 mg h⁻¹ cm⁻², which showed an excellent performance compared with other reported works. The influential factors in electrocatalytic 2e⁻ ORR were profoundly discussed from the perspective of thermodynamics and electrochemical interface, particularly emphasizing on alkaline affinity of developed electrocatalytic system, which was extrapolated to a beneficial outer-sphere electron transfer pathway, variation on adsorption strength of oxygenated species and working electrode potential range. Finally, long-term operation stability and successful application in the Electro-Fenton process indicated great potential of developed system for H₂O₂ synthesis and environmental remediation.

CRediT authorship contribution statement

Mingran Li¹: Writing - Original Draft, Investigation, Methodology, Formal analysis, Validation, Software, Data Curation, Visualization. **Huachun Lan**^a: Writing - Review & Editing, Conceptualization, Methodology, Resources. **Xiaoqiang An**^a: Conceptualization, Methodology, Resources, Project administration. **Xia Qin**^{*}: Writing - Review & Editing, Conceptualization, Supervision, Project administration, Resources, Funding acquisition. **Zilong Zhang**^g: Investigation, Validation, Software. **Tinghui Li**^g: Formal analysis, Data Curation.

Declaration of Competing Interest

The authors declare that they have no known competing financial interests or personal relationships that could have appeared to influence the work reported in this paper.

Data availability

Data will be made available on request.

Acknowledgments

The fund of conducting research and preparation of the article was supported by the National Natural Science Foundation of China (No. 51478009) and Double First Class University Plan (No. 005000541221511).

Appendix A. Supporting information

Supplementary data associated with this article can be found in the online version at [doi:10.1016/j.apcatb.2023.123125](https://doi.org/10.1016/j.apcatb.2023.123125).

References

- [1] Q.Z. Zhang, M.H. Zhou, G.B. Ren, Y.W. Li, Y.C. Li, X.D. Du, Highly efficient electrosynthesis of hydrogen peroxide on a superhydrophobic three-phase interface by natural air diffusion, *Nat. Commun.* 11 (2020).
- [2] J. Zhou, X.Q. An, H.C. Lan, H.J. Liu, J.H. Qu, New insights into the surface-dependent activity of graphitic felts for the electro-generation of H₂O₂, *Appl. Surf. Sci.* 509 (2020).
- [3] N. Ramaswamy, S. Mukerjee, Influence of inner- and outer-sphere electron transfer mechanisms during electrocatalysis of oxygen reduction in alkaline media, *J. Phys. Chem. C* 115 (2011) 18015–18026.
- [4] Y. Jiang, P. Ni, C. Chen, Y. Lu, P. Yang, B. Kong, A. Fisher, X. Wang, Selective electrochemical H₂O₂ production through two-electron oxygen electrochemistry, *Adv. Energy Mater.* 8 (2018).
- [5] E. Mitraka, M. Grysziel, M. Vagin, M.J. Jafari, A. Singh, M. Warczak, M. Mitrakas, M. Berggren, T. Ederth, I. Zozoulenko, X. Crispin, E.D. Glowacki, Electrocatalytic production of hydrogen peroxide with Poly(3,4-ethylenedioxythiophene) electrodes, *Adv. Sustain. Syst.* 3 (2019).
- [6] S. Fukuzumi, Y.-M. Lee, W. Nam, Solar-driven production of hydrogen peroxide from water and dioxygen, *Chem. -a Eur. J.* 24 (2018) 5016 (+).
- [7] H. Sheng, A.N. Janes, R.D. Ross, D. Kaiman, J. Huang, B. Song, J.R. Schmidt, S. Jin, Stable and selective electrosynthesis of hydrogen peroxide and the electro-Fenton process on CoSe₂ polymorph catalysts, *Energy Environ. Sci.* 13 (2020) 4189–4203.
- [8] Y. Xia, H. Shang, Q. Zhang, Y. Zhou, X. Hu, Electrogenation of hydrogen peroxide using phosphorus-doped carbon nanotubes gas diffusion electrodes and its application in electro-Fenton, *J. Electroanal. Chem.* 840 (2019) 400–408.
- [9] D. Iglesias, A. Giuliani, M. Melchionna, S. Marchesan, A. Criado, L. Nasi, M. Bevilacqua, C. Tavagnacco, F. Vizza, M. Prato, P. Fornasiero, N-doped graphitized carbon nanohorns as a forefront electrocatalyst in highly selective O₂ reduction to H₂O₂, *Chem* 4 (2018) 106–123.
- [10] Y. Liu, X. Quan, X. Fan, H. Wang, S. Chen, High-yield electrosynthesis of hydrogen peroxide from oxygen reduction by hierarchically porous carbon, *Angew. Chem. -Int. Ed.* 54 (2015) 6837–6841.
- [11] W. Yang, M. Zhou, J. Cai, L. Liang, G. Ren, L. Jiang, Ultrahigh yield of hydrogen peroxide on graphite felt cathode modified with electrochemically exfoliated graphene, *J. Mater. Chem. A* 5 (2017) 8070–8080.
- [12] M. Li, X. Qin, Enhanced in-situ electrosynthesis of hydrogen peroxide on a modified active carbon fiber prepared through response surface methodology, *J. Electroanal. Chem.* (2022), 116241.
- [13] M.R. Li, X. Qin, M.X. Gao, T.H. Li, Y. Lv, Graphitic carbon nitride and carbon nanotubes modified active carbon fiber cathode with enhanced H₂O₂ production and recycle of Fe³⁺/Fe²⁺ for electro-Fenton treatment of landfill leachate concentrate, *Environ. Sci. -Nano* 9 (2022) 632–652.
- [14] M. Hou, Y. Chu, X. Li, H. Wang, W. Yao, G. Yu, S. Murayama, Y. Wang, Electro-peroxide degradation of diethyl phthalate: cathode selection, operational parameters, and degradation mechanisms, *J. Hazard. Mater.* 319 (2016) 61–68.
- [15] Y. Zheng, Y. Jiao, J. Chen, J. Liu, J. Liang, A. Du, W. Zhang, Z. Zhu, S.C. Smith, M. Jaroniec, G.Q. Lu, S.Z. Qiao, Nanoporous graphitic-C₃N₄@carbon metal-free electrocatalysts for highly efficient oxygen reduction, *J. Am. Chem. Soc.* 133 (2011) 20116–20119.
- [16] J. Geng, H. Zhang, Z. Zhang, J. Gao, S. Wang, X. Hu, J. Li, Enhanced electro-Fenton oxidation by introducing three-phase interface with simultaneous optimization of O₂ and pollutant transfer for effective tetracycline hydrochloride removal, *Chem. Eng. J.* 450 (2022), 137891.
- [17] Y. Li, Y. Zhang, G. Xia, J. Zhan, G. Yu, Y. Wang, Evaluation of the technoeconomic feasibility of electrochemical hydrogen peroxide production for decentralized water treatment, *Front. Environ. Sci. Eng.* 15 (2021).
- [18] O. Scialdone, A. Galia, C. Gattuso, S. Sabatino, B. Schiavo, Effect of air pressure on the electro-generation of H₂O₂ and the abatement of organic pollutants in water by electro-Fenton process, *Electrochim. Acta* 182 (2015) 775–780.
- [19] P. Han, D.M. Bartels, Temperature dependence of oxygen diffusion in H₂O and D₂O, *J. Phys. Chem.* 100 (1996) 5597–5602.
- [20] Y.S. Zheng, J.G. He, S. Qiu, D.H. Yu, Y.S. Zhu, H.L. Pang, J. Zhang, Boosting hydrogen peroxide accumulation by a novel air-breathing gas diffusion electrode in electro-Fenton system, *Appl. Catal. B-Environ.* 316 (2022).
- [21] J.F. Perez, J. Llanos, C. Saez, C. Lopez, P. Canizares, M.A. Rodrigo, The jet aerator as oxygen supplier for the electrochemical generation of H₂O₂, *Electrochim. Acta* 246 (2017) 466–474.
- [22] W. Zhou, X.X. Meng, L. Rajic, Y.F. Xue, S. Chen, Y.N. Ding, K.K. Kou, Y. Wang, J. H. Gao, Y.K. Qin, A.N. Alshawabkeh, "Floating" cathode for efficient H₂O₂ electrogeneration applied to degradation of ibuprofen as a model pollutant, *Electrochem. Commun.* 96 (2018) 37–41.
- [23] S. Qiu, W.W. Tang, S.L. Yang, J.Y. Xie, D.F. Yu, O. Garcia-Rodriguez, J.H. Qu, S. N. Bai, F.X. Deng, J. Radjenovic, A microbubble-assisted rotary tubular titanium cathode for boosting Fenton's reagents in the electro-Fenton process, *J. Hazard. Mater.* 424 (2022).
- [24] T. Perez, G. Coria, I. Sires, J.L. Nava, A.R. Uribe, Electrosynthesis of hydrogen peroxide in a filter-press flow cell using graphite felt as air-diffusion cathode, *J. Electroanal. Chem.* 812 (2018) 54–58.
- [25] J. Liang, Q. Xiang, W. Lei, Y. Zhang, J. Sun, H. Zhu, S. Wang, Ferric iron reduction reaction electro-Fenton with gas diffusion device: A novel strategy for improvement of comprehensive efficiency in electro-Fenton, *412* (2021) 125195.
- [26] J.X. Geng, H.C. Zhang, Z.H. Zhang, J.X. Gao, S.B. Wang, X.Y. Hu, J. Li, Enhanced electro-Fenton oxidation by introducing three-phase interface with simultaneous optimization of O₂ and pollutant transfer for effective tetracycline hydrochloride removal, *Chem. Eng. J.* 450 (2022).
- [27] M. Li, X. Qin, J. Cui, R. Guo, C. Guo, Z. Wang, T. Li, Three-dimensional Electro-Fenton degradation for fulvic acids with Cu-Fe bimetallic aerogel-like carbon as particle electrode and catalyst: electrode preparation, operation parameter optimization and mechanism, *J. Environ. Chem. Eng.* 9 (2021).
- [28] Z. He, J. Chen, Y. Chen, C.P. Makwarimba, X. Huang, S. Zhang, J. Chen, S. Song, An activated carbon fiber-supported graphite carbon nitride for effective electro-Fenton process, *Electrochim. Acta* 276 (2018) 377–388.
- [29] A.H.A.M. Videla, L. Zhang, J. Kim, J. Zeng, C. Francia, J. Zhang, S. Specchia, Mesoporous carbons supported non-noble metal Fe-N (X) electrocatalysts for PEM fuel cell oxygen reduction reaction, *J. Appl. Electrochem* 43 (2013) 159–169.
- [30] S. Maldonado, K.J. Stevenson, Influence of nitrogen doping on oxygen reduction electrocatalysis at carbon nanofiber electrodes, *J. Phys. Chem. B* 109 (2005) 4707–4716.
- [31] H. Xu, H. Guo, C. Chai, N. Li, X. Lin, W. Xu, Anodized graphite felt as an efficient cathode for in-situ hydrogen peroxide production and Electro-Fenton degradation of rhodamine B, *Chemosphere* 286 (2022).
- [32] D. Guo, R. Shibuya, A. Akiba, S. Saji, T. Kondo, J. Nakamura, Active sites of nitrogen-doped carbon materials for oxygen reduction reaction clarified using model catalysts, *351* (2016) 361–365.
- [33] T. Kondo, S. Casolo, T. Suzuki, T. Shikano, M. Sakurai, Y. Harada, M. Saito, M. Oshima, M.I. Trioni, G.F. Tantardini, J. Nakamura, Atomic-scale characterization of nitrogen-doped graphite: effects of dopant nitrogen on the local electronic structure of the surrounding carbon atoms, *Phys. Rev. B* 86 (2012).
- [34] J. Zhang, G. Zhang, S. Jin, Y. Zhou, Q. Ji, H. Lan, H. Liu, J. Qu, Graphitic N in nitrogen-doped carbon promotes hydrogen peroxide synthesis from electrocatalytic oxygen reduction, *Carbon* 163 (2020) 154–161.
- [35] G.-L. Chai, Z. Hou, T. Ikeda, K. Terakura, Two-electron oxygen reduction on carbon materials catalysts: mechanisms and active sites, *J. Phys. Chem. C* 121 (2017) 14524–14533.
- [36] Y. Zhu, F. Deng, S. Qiu, F. Ma, Y. Zheng, R. Lian, Enhanced electro-Fenton degradation of sulfonamides using the N, S co-doped cathode: Mechanism for H₂O₂ formation and pollutants decay, *J. Hazard. Mater.* 403 (2021), 123950.
- [37] P. Ding, L. Cui, D. Li, W. Jing, Innovative dual-compartment flow reactor coupled with a gas diffusion electrode for in situ generation of H₂O₂, *Ind. Eng. Chem. Res.* 58 (2019) 6925–6932.
- [38] T. Temesgen, T.T. Bui, M. Han, T.I. Kim, H. Park, Micro and nanobubble technologies as a new horizon for water-treatment techniques: a review, *Adv. Colloid Interface Sci.* 246 (2017) 40–51.
- [39] I. Katsounaros, W.B. Schneider, J.C. Meier, U. Benedikt, P.U. Biedermann, A.A. Auer, K.J.J. Mayrhofer, Hydrogen peroxide electrochemistry on platinum: towards understanding the oxygen reduction reaction mechanism, *14*, 2012 pp. 7384–7391.
- [40] S.R. Logan, The Arrhenius equation revisited, *J. Chem. Educ.* 76 (1999), 899–899.
- [41] J.S. Spendlow, A. Wieckowski, Electrocatalysis of oxygen reduction and small alcohol oxidation in alkaline media, *CPCCP* 9 (2007) 2654–2675.
- [42] M. Li, X. Qin, M. Gao, T. Li, Y. Lv, Enhanced in-situ electrosynthesis of hydrogen peroxide on a modified active carbon fiber prepared through response surface methodology, *J. Electroanal. Chem.* 912 (2022).
- [43] S. Qiu, W. Tang, S. Yang, J. Xie, D. Yu, O. Garcia-Rodriguez, J. Qu, S. Bai, F. Deng, J. Radjenovic, A microbubble-assisted rotary tubular titanium cathode for boosting Fenton's reagents in the electro-Fenton process, *J. Hazard. Mater.* 424 (2022).
- [44] B.E. Conway, Electrochemical oxide film formation at noble metals as a surface-chemical process, *49* (1995) 331–452.
- [45] N. Markovic, H. Gasteiger, P.N. Ross, Kinetics of oxygen reduction on Pt(hkl) electrodes: implications for the crystallite size effect with supported Pt electrocatalysts, *J. Electrochem. Soc.* 144 (1997) 1591.
- [46] N. Wakabayashi, F. Kitamura, T. Ohsaka, K. Tokuda, Effect of adsorbed anions on the outer-sphere electron-transfer reactions of cobalt complexes at platinum single-crystal electrodes, *J. Electroanal. Chem.* 499 (2001) 161–168.
- [47] K.-D. Liss, K. Chen, Frontiers of synchrotron research in materials science, *MRS Bull.* 41 (2016) 435–444.
- [48] J.S. Spendlow, A. Wieckowski, Electrocatalysis of oxygen reduction and small alcohol oxidation in alkaline media, *9* (2007) 2654–2675.
- [49] A.J. Appleby, Electrocatalysis, in: B.E. Conway, J.O.M. Bockris, E. Yeager, S.U. M. Khan, R.E. White (Eds.), *Comprehensive Treatise of Electrochemistry: Volume 7 Kinetics and Mechanisms of Electrode Processes*, Springer US, Boston, MA, 1983, pp. 173–239.
- [50] N. Sutin, Marcus contributions to electron-transfer theory, *J. Phys. Chem.* 90 (1986) 3465–3466.
- [51] J. Weber, Fluctuation dissipation theorem, *Phys. Rev.* 101 (1956) 1620–1626.
- [52] J.C. Lewis, Einstein-Stokes diffusion-coefficient for brownian motion in 2 dimensions, *Phys. Lett. A*, A 44 (1973) 245–246.
- [53] E.J. Taylor, N.R.K. Vilambi, A. Gelb, The nature of the catalytic peak for oxygen reduction in alkaline electrolyte on the Au(100) surface, *J. Electrochem. Soc.* 136 (1989) 1939.
- [54] C. Zhang, F.-R.F. Fan, A.J. Bard, Electrochemistry of oxygen in concentrated NaOH solutions: solubility, diffusion coefficients, and superoxide formation, *J. Am. Chem. Soc.* 131 (2009) 177–181.
- [55] L. Zhou, Z. Hu, C. Zhang, Z. Bi, T. Jin, M. Zhou, Electrogenation of hydrogen peroxide for electro-Fenton system by oxygen reduction using chemically modified graphite felt cathode, *Sep. Purif. Technol.* 111 (2013) 131–136.
- [56] L. Zhou, M. Zhou, Z. Hu, Z. Bi, K.G. Serrano, Chemically modified graphite felt as an efficient cathode in electro-Fenton for p-nitrophenol degradation, *Electrochim. Acta* 140 (2014) 376–383.

- [57] J. Zhou, X. An, H. Lan, H. Liu, J. Qu, New insights into the surface-dependent activity of graphitic felts for the electro-generation of H₂O₂, *Appl. Surf. Sci.* 509 (2020).
- [58] B. Ou, J. Wang, Y. Wu, S. Zhao, Z. Wang, Degradation of aniline by photoelectro-Fenton process using g-C₃N₄ based cathode, *J. Electroanal. Chem.* 848 (2019), 113273.
- [59] M. Zarei, D. Salari, A. Niaei, A. Khataee, Peroxi-coagulation degradation of C.I. Basic Yellow 2 based on carbon-PTFE and carbon nanotube-PTFE electrodes as cathode, *Electrochim. Acta* 54 (2009) 6651–6660.
- [60] Z. Pan, K. Wang, Y. Wang, P. Tsiakaras, S. Song, In-situ electrosynthesis of hydrogen peroxide and wastewater treatment application: a novel strategy for graphite felt activation, *Appl. Catal. B: Environ.* 237 (2018) 392–400.
- [61] L. Zhou, M. Zhou, C. Zhang, Y. Jiang, Z. Bi, J. Yang, Electro-Fenton degradation of p-nitrophenol using the anodized graphite felts, *Chem. Eng. J.* 233 (2013) 185–192.
- [62] A.D. Pozzo, L. Di Palma, C. Merli, E. Petrucci, An experimental comparison of a graphite electrode and a gas diffusion electrode for the cathodic production of hydrogen peroxide, 35 (2005) 413–419.
- [63] D. Salari, A. Niaei, A. Khataee, M. Zarei, Electrochemical treatment of dye solution containing C.I. Basic Yellow 2 by the peroxi-coagulation method and modeling of experimental results by artificial neural networks, *J. Electroanal. Chem.* 629 (2009) 117–125.
- [64] X. Lu, M. Zhou, Y. Li, P. Su, J. Cai, Y. Pan, Improving the yield of hydrogen peroxide on gas diffusion electrode modified with tert-butyl-anthraquinone on different carbon support, 320 (2019) 134552.
- [65] D. Li, T. Zheng, Y. Liu, D. Hou, K.K. Yao, W. Zhang, H. Song, H. He, W. Shi, L. Wang, J. Ma, A novel Electro-Fenton process characterized by aeration from inside a graphite felt electrode with enhanced electrogeneration of H₂O₂ and cycle of Fe³⁺/Fe²⁺, *J. Hazard. Mater.* 396 (2020), 122591.